Modelling of critical defect distributions for estimating the size effect of selective laser melted 316L stainless steel

Tomasz Tomaszewski*

Faculty of Mechanical Engineering, University of Science and Technology

al. Prof. S. Kaliskiego 7, 85-796 Bydgoszcz, Poland

Abstract

The paper presents modelling the effect of specimen size on the fatigue behaviour of SLM 316L stainless steel. The failure mechanism assumes an important role in fatigue crack initiated from random material defects. The finite element calculations showed an increase in the non-local stress distribution of the Crossland criterion for varying defect location and size. A procedure for generating critical defects in a highly stressed volume is proposed to simulate the distributions of extreme values of equivalent stress and material sensitivity coefficient for size effect. The predicted fatigue strength for selected defect size distribution parameters correlates well with experimental data.

Keywords

Additive manufacturing; High-cycle fatigue; Size effect; Crossland criterion; Highly stressed volume; Weibull distribution

Nomenclature

$\sqrt{area}$	Murakami defect size parameter
μ	normal distribution size parameter
a	crack depth
A	min. cross-sectional area of a specimen
A_0	min. cross-sectional area of a reference specimen
a_f	final crack depth
a_i	initiated crack depth
a_{ij}	coefficients of a polynomial
A_s	longitudinal elongation
C_p	Paris law material constant

*Corresponding author: tomaszewski@pbs.edu.pl

d_l	Murakami location of a defect
E	modulus of elasticity
F	axial force in a RVE model
F_p	function of geometry and a relative crack length
HSV	highly stressed volume
HV	Vickers hardness
$J_{1,max}$	max. hydrostatic stress over a load cycle
$J_{2,a}$	amplitudes of the second invariant of a deviatoric stress tensor over a load cycle
k,b	linear regression coefficients
K_t	theoretical stress concentration factor
L	longitudinal elongation
l	specimen edge
l_c	distance of a crack from a specimen centre
l_s	overall specimen length
m_p	Paris law exponent
N	number of cycles
n	number of specimens
$n\%$	highly stressed parameter
n_d	number of defects
N_f	number of cycles to failure
N_i	number of cycles for initiation
N_p	number of cycles for propagation
n_s	size effect coefficient
n_{sCR}	size effect coefficient for normalized Crossland stress
P	cumulative distribution function
P_f	failure probability
R	stress ratio
$R_{0.2}$	yield strength
R^2	determination coefficient
R_f	radius of fillet

R_m	tensile strength
$\bar{\bar{S}}$	cyclic stress deviator tensor at two instantaneous times (t_I, t_J)
S_a	stress amplitude
S_f	fatigue strength for knee point (P_f = 50%)
$S_{pred.}$	predicted fatigue strength
t	specimen thickness
t_b	min. thickness between a specimen outer surface and defect
t_d	max. thickness between a specimen outer surface and defect
t_i	distance between defects
V_d	average defect volume
w_1	min. specimen width
w_2	width of a specimen grip section
Z	reduction of area
α	Weibull distribution shape parameter
α_0	significance level of a confidence interval
α_{CR}, β_{CR}	material parameters of the Crosslands criterion
α_M	exponent of the Murakami equation
β_0 - β_5	non-linear regression coefficients
δ	Weibull distribution scale parameter
ΔK	stress intensity factor range
ΔK_{th}	long crack threshold stress intensity factor range
ΔS	stress range
da/dN	crack propagation rate
λ	Weibull distribution location parameter
ρ_d	defect distribution density
σ	normal distribution shape parameter
$\bar{\bar{\sigma}}$	stress tensor
σ_{CR}	Crossland equivalent stress
$\sigma_{CR,n}$	normalized Crossland equivalent stress
$\sigma_{CR,n\ max}$	normalized Crossland equivalent stress for critical defect

σ_{max} max. normal stress

σ_n normal stress

σ_w fatigue strength at a knee point of fully reversed tension/compression

τ_w fatigue strength at a knee point of fully reversed torsion

1. Introduction

It is well known that the fatigue strength of a material depends on the size of the object. Most authors of experimental studies have confirmed that smaller specimens have higher strength, which is true on a macro scale. As the specimen size approaches the grain size, other failure mechanisms (plastic strain gradient, dislocation slip) can be observed, which introduce discrepancies between results for different scale ranges. The fatigue strength on a macro scale depends on categorised factors, including the random distribution of material defects (statistical size effect), the specimen shape and type of load (geometric size effect) and the technological processes used to manufacture the object (technological size effect) [1]. The origin of the size effect is the natural limitation of scaling all product properties to a constant level (e.g. material structure, defect distribution, surface layer). The scaling procedures used as defined by similarity theory assume a proportional change in the dimensions relevant to the process under analysis [2].

Regardless of the origin of the size effect, an important factor influencing the fatigue behaviour is the inhomogeneity of the structure manifested by the occurrence of random material defects distributed in the elementary unit of the material [3]. A common cause of failure of additively manufactured metallic materials is the formation of defects (pores, unmelted particles) [4-11]. The decrease in fatigue life of a larger specimen can be related to the defects size formed by the lack of fusion layers and incomplete bonding between melt pools. The resulting defects cause local discontinuities in the structure and stress concentrations causing local plastic deformation in the form of slip bands. The initiated crack propagates with the number of cycles. The resulting propagation region determines the length of the final crack depending on the stress amplitude [12, 13]. As a result, the fatigue failure process is a continuous phenomenon involving crack initiation and propagation. The evaluation of the size effect is carried out for each phase of failure. Due to the difficulty of determining the limit value of the initiation phase, the smallest crack depth at which linear elastic fracture mechanics (LEFM) can be applied is assumed [14]. In terms of the analyses conducted, most of the fatigue life is consumed by crack initiation [15, 16]. The size effect approaches depend the model on the failure mechanism determining the initiation phase.

A commonly used model to assess the failure probability depending on size is the weakest link theory proposed by Weibull [17]. The assumption of the model is the presence of a critical defect in a statistical population of data.

The initiation and propagation of the crack in the different areas of the object is independent of each other. The location of a critical defect depends on the loading conditions and the geometry of the object, so methods are used to limit this area to a highly stressed volume [18]. The approach allows for the determination of a volume above an assumed percentage of maximum stress, characterised by a high probability of a critical defect. Therefore, *HSV* is combined with the Weibull model [19]. The critical defect detected in a given volume is analysed in the context of a defined specimen population. The resulting defect size distribution is described by extreme value statistics [20]. Another attempt to explain material heterogeneity involves modelling the size effect with a 'lacunar' fractal set. The material properties are estimated using renormalisation procedures for the fractal dimension of the damaged heterogeneous ligament or fracture surface [21]. The deterministic size effect models are most commonly used in engineering calculations, extrapolating test results from laboratory specimen sizes to the real object [22].

The paper proposes a size effect model for estimating the fatigue behaviour of SLM 316L stainless steel. The location of the *P-S-N* curves is estimated depending on the parameters of the defect size distribution in *HSV*. The failure mechanism assumes the presence of a defect and a local multi-axial stress state. The criticality of a defect is defined by the Crossland fatigue criterion [23] depending on the size and the location of the defect relative to the surface. Other factors such as the shape of the defect and its change under load also influence the stress distribution around the defect. Small deviations from the assumed geometry can significantly affect the stress concentration factor [3]. Due to the difficulty in accurately determining the parameters indicated, quantitative modelling of the stress distribution assumes the use of generally accepted simplifications. In an object volume subjected to time-varying load, the distributions of defects, cracks, changes in structure or local material properties are consistent with extreme value statistics [24]. Using a probabilistic approach for the material data taken, fatigue criteria and statistical methods it is possible to estimate the fatigue strength for a variable size.

2. Experimental procedure

2.1. Material

The material tested is 316L stainless steel for additive manufacturing supplied as an atomized spherical powder. Fig. 1 shows the log-normal distribution of powder particle size. The confidence interval for the 0.05 significance level ranges from 28.2 μm to 64.1 μm. The average particle size is equal to 44.8 μm. The chemical composition of powder contains *wt.*% by mass: 0.03 C; 1.00 Si; 2.00 Mn; 0.03 S; 0.04 P; 16-18 Cr; 10-14 Ni; 2-3 Mo.

The specimens were manufactured in selective laser melting using a SLM 125HL machine (SLM Solutions GmbH) under argon gas shielding. The powder melting and fusion was performed using a 200 W laser power, with a hatching pitch of 0.12 mm, scanning speed of 800 mm/s. The specimens were built with layers 0.03 mm

thick. The energy density of the parameters used was 69.4 J/mm^3. The software created laser scan path determined non-unidirectional oriented stresses due to thermal contraction. An as-built heat treatment was not applied. All specimens were manufactured on a single build plate (Fig. 2). The manufacturing required the preparation of 3D models saved as stereolithographic objects in STL format. The necessity to generate support structures between the specimen and build plate determined the use of machining. The horizontal build orientation used was dictated by the most advantageous mechanical properties declared by the producer. The location of the specimens on the build plate determined to minimize the impact of splatter or subsequent layering. The details of the specimen geometries are provided in Section 2.2.

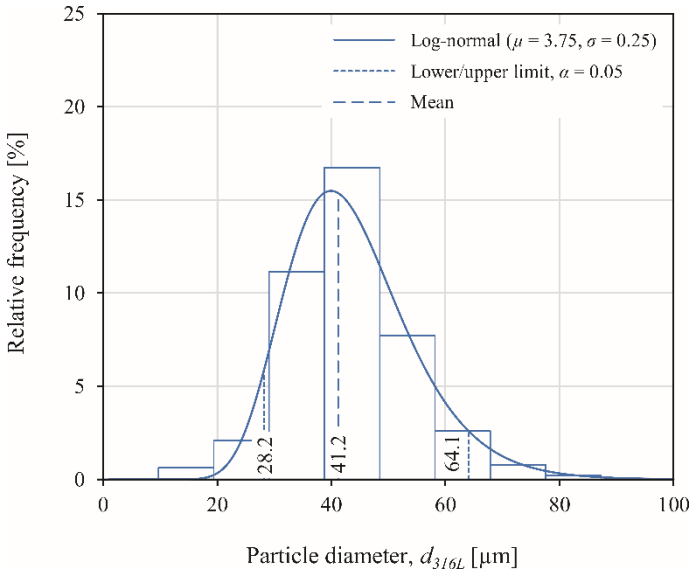

Fig. 1. Log-normal distribution of SLM 316L stainless steel powder particle size.

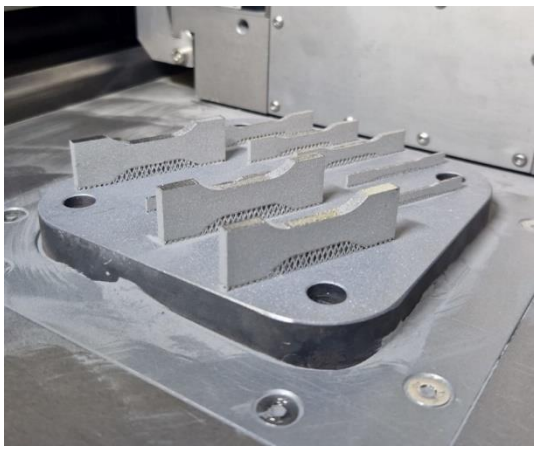

Fig. 2. Example view of horizontally oriented specimens on the build plate of the SLM 125HL machine.

The identification of mechanical properties was performed in a static tensile test in accordance with the standard [25]. The dimensions of the specimens were in line with the fatigue test specimens (Fig. 4, Table 2), using a modification for a working part of length (15 mm). Fig. 3 shows engineering stress-strain curves for varying

specimen size. Table 1 summarizes the mean values calculated for the three specimens and the standard deviation. Due to the lack of a clear yield stress, the standard 0.2% offset was used. The tensile strain resulted in defined plasticity, followed by moderate strain hardening. The curve over the strain for the tensile strength determines a noticeable decrease in stress until failure. A strongly decrease in ductility tensile elongation is observed as the specimen size decreases. The values are 17.0% and 43.6% lower than the largest specimen (A32), respectively for A08, A02. Only the necking part of the stress-strain curve is dependent on the specimen dimensions. The phenomenon determines the mechanical effect, not the pure size effect under fatigue failure. A slight decrease in tensile strength and yield strength with the size is observed.

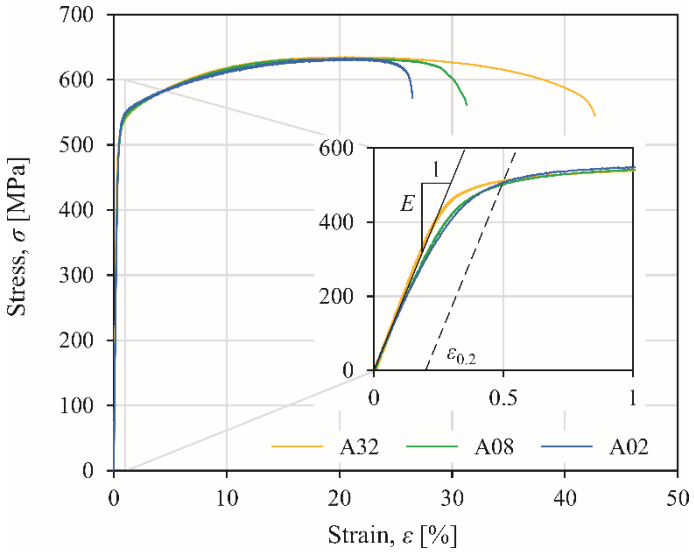

Fig. 3. Engineering stress-strain curves of SLM 316L for various specimen size.

Table 1. Mechanical properties of SLM 316L for various specimen size.

Specimen number	Min. cross-sectional area, A [mm^2]	Modulus of elasticity, E [GPa]	Tensile strength, R_m [MPa]	Yield strength, $R_{0.2}$ [MPa]	Longitudinal elongation, L [%]
A02	2	164 ± 5	634 ± 6	507 ± 5	24.0 ± 2.1
A08	8	168 ± 4	637 ± 4	502 ± 8	35.4 ± 3.0
A32	32	172 ± 5	641 ± 6	518 ± 9	42.6 ± 0.5

2.2. Fatigue tests conditions

The high-cycle fatigue tests under uniaxial, sinusoidal loading were carried out by standards [26, 27]. Fig. 4 shows the geometry of a flat specimen with a variable working part used in fatigue tests. The experimental test programme involves verifying the size effect for varying specimen sizes. Table 2 contains the dimensions of the geometry. All specimens were additively manufactured in a single build plate. The working part across the width of the specimen was machined due to the necessity of removing the supports. The width of the minimum section

w_1, thickness t, radius of the rounding R_f change proportionally. The theoretical stress concentration factor K_t is constant. The dimensional dependencies were used to eliminate the effect of other factors on the results.

The tests were carried out for an symmetrical cycle (R = -1) and an average frequency of 20 Hz. The end criterion for the fatigue tests was the propagation of one continuous crack perpendicular to the load axis. The tests aimed to determine the *P-S-N* curves in terms of high-cycle fatigue for the load-controlled test. The upper load range was determined significantly below the experimentally determined lowest yield point. The lower test range for determining the knee point of the fatigue characteristic is assumed to be $5 \cdot 10^5$ cycles [28]. All experimental tests were performed on an Instron 8874 (Instron GmbH) materials testing machine with a ± 25 kN force gauge and a 2620 Instron dynamic extensometer with a 12.5 mm gauge base length and ± 5 mm extension.

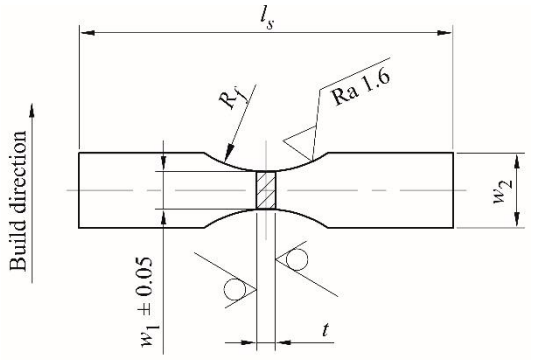

(a)

(b)

Fig. 4. Geometry of the unnotched stress-controlled fatigue test specimens made of SLM 316L stainless steel: a) dimensional drawing, b) actual view.

Table 2. Specimen dimensions for variable size (K_t = const).

Specimen number	Dimension, [mm]					Min. cross-sectional area, A [mm^2]	Number of specimens, n
	w_1	w_2	t	R_f	l_s		
A02	2	4	1	6	30	2	9
A08	4	8	2	12	35	8	9
A32	8	16	4	24	50	32	10

2.3. High-cycle fatigue results

The classical approach of approximating experimental data for high-cycle fatigue assumes the determination of the *S-N* field. It is well known that the scatter of data for fatigue life is larger at lower stress amplitudes. The model implies discrepancies that determine parallel failure/survival probability curves. The extrapolation of the experimental data to any percentage curve is represented by the *P-S-N* curves. The experimental points are approximated using a probabilistic model based on a three-parameter Weibull cumulative distribution function for a chosen failure probability P_f, as follows [17]:

$$P_f(N_f, S_f) = 1 - \exp\left[-\left(\frac{(N_f, S_f) - \lambda}{\delta}\right)^{\alpha}\right] \quad (1)$$

where N_f is the number of cycles to failure, S_f is the fatigue strength, α is the shape parameter, δ is the scale parameter, λ is the location parameter.

a shows the approximated *P-S-N* curves in the bi-logarithmic system for a variable specimen size. The dashed and dotted lines correspond to the failure probability, 50%, 10% and 90% respectively. The vertical dashed line marks the number of cycles for the knee point of the curves. The location of the experimental points identifies the number of cycles N_f for the applied stress amplitude S_a. The diameter of the points determines the measured defect size (Murakami parameter $\sqrt{area}$ [3]) of the fatigue crack initiation. The parameter is defined as the square root of the defect area projected onto a perpendicular plane to the applied maximum principal stress. A detailed analysis of the effect of selected defect parameters (size, location) is provided in Section 3. Fig. 5b shows the cumulative distribution function for $5 \cdot 10^5$ cycles. The points represent the estimated failure probability based on Weibull distribution. The size effect is independent of failure probability. The significant differences in the decrease in fatigue life with specimen size for the extreme P_f levels were not observed. Table 3 contains the estimated Weibull distribution parameters and the fatigue strength for the selected failure probability. The scale parameter δ increases with a decrease in the specimen size, which indicates obtaining higher fatigue life distributions for a smaller specimen. A quantitative measure of a material's sensitivity to the size effect (coefficient n_s) is the ratio of the fatigue strength for any specimen size $S_{f,A}$ and a reference specimen $S_{f,A0}$. Due to the advantages of testing on miniature specimens [29], the reference fatigue strength distribution S_{A0} was determined for the specimen (A08). The selection of the reference size determines the no significant differences in fatigue strength for the smallest specimens. The coefficient n_s (Table 3) is calculated for the same percentage curves corresponding to the number of cycles for the knee point. The coefficient n_s decreases as the specimen size increases. The material behaviour is expected and consistent with theoretical assumptions.

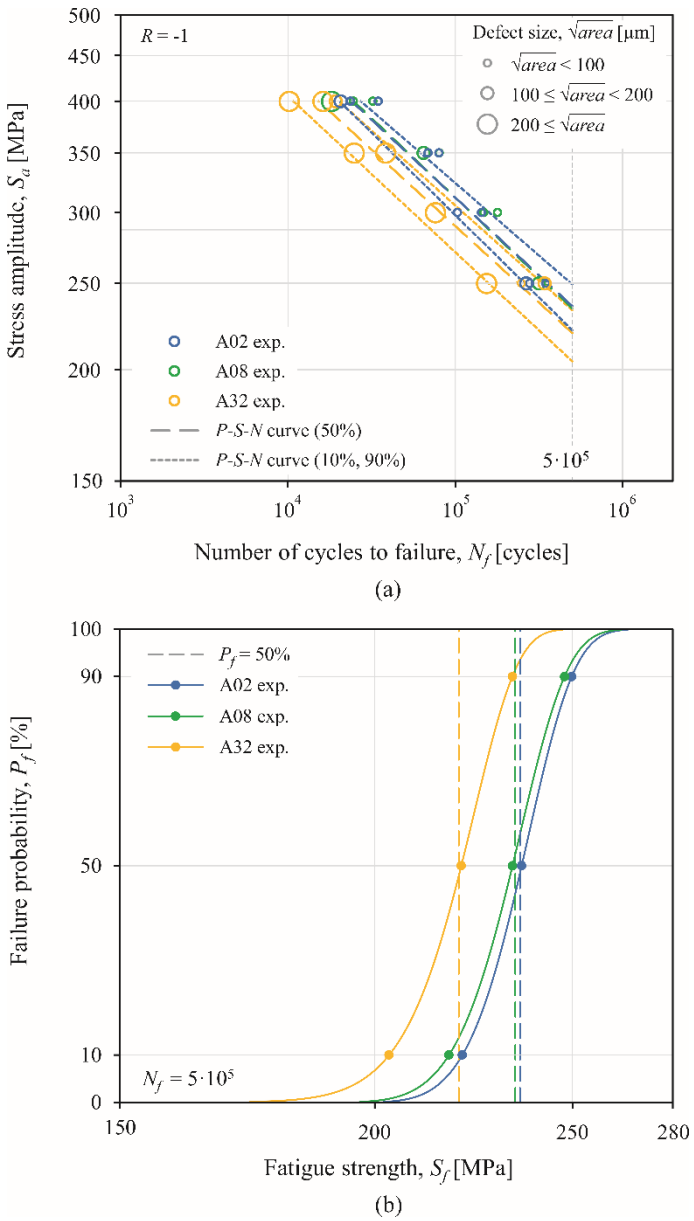

Fig. 5. Experimental results of high-cycle fatigue tests for variable size specimens made of SLM 316L steel: a) *P-S-N* curves, b) Weibull cumulative distribution function for fatigue life $5 \cdot 10^5$ cycles.

Table 3. Results of *P-S-N* curve approximation for fatigue life $5 \cdot 10^5$ cycles of a Weibull distribution.

Specimen number	Weibull distribution			Failure probability, P_f [%]	Fatigue strength, S_f [MPa]	Size effect coefficient, $n_s = S_{f,A}/S_{f,A0}$
	Location parameter, λ	Shape parameter, α	Scale parameter, δ			
A02 (*A*)	191.9	4.4	47.9	10	220.6	1.014
				50	235.9	1.009
				90	249.8	1.008
A08 (A_0)	183.9	4.8	53.7	10	217.5	1
				50	233.6	
				90	247.7	
A32 (*A*)	131.4	8.8	92.9	10	203.3	0.934
				50	220.5	0.943
				90	233.5	0.942

2.4. Fatigue initiation life

The failure mechanism estimation of SLM 316L steel determining the location of the *P-S-N* curve was carried out for the crack initiation and propagation phases. The propagation rate of a long crack is characterized by Paris' Law. The fracture mechanics equations used require knowledge, in addition to stress and crack size, of the driving force of crack propagation. As a result, two material parameters are required: C_P and m_P. The stable crack growth phase defined by a linear elastic fracture mechanics model (LEFM) in the following form:

$$\frac{da}{dN} = C_p(\Delta K)^{m_p} \tag{2}$$

where a is the crack depth, N is the number of cycles, C_p, m_p are the material constant. The effective range of the stress intensity factor is determined from the equation [30]:

$$\Delta K = F_p \Delta S_f \sqrt{\pi a} \tag{3}$$

where ΔS_f is the stress range, F_p is the function of geometry and the relative crack length. The calculation of the fatigue life for the propagation phase implies integration of the equation from the initial to the final crack length, according to the equation:

$$N_p = \int_{a_i}^{a_f} \frac{da}{C\left(F_p \Delta S \sqrt{\pi a}\right)^m} \tag{4}$$

where N_p is the crack propagation life, a_i is the shortest crack length completing the initiation phase in LEFM, a_f is the final crack length representing the value for the brittle fracture region of the fracture surface. The fatigue life of the initiation phase (N_i) is calculated by subtracting the total number of cycles (N_f) from the value in Eq. (4). The value of a_i is the limiting length between the crack initiation and propagation phases [31]. The exact determination of this value is difficult due to the correctness of defining the length of the crack ending the initiation phase [32]. The assumption of a too short crack can be a threat to the correct implementation of linear elastic fracture mechanics due to the local plasticity of the notch. For too long a crack, the deformation of the notch surface is not used for a large distance from the notch [30]. From an engineering point of view, the value of a_i is assumed to be less than 1 mm [33]. The limit value is equal to the size of the defect [34] or 10 times the diameter equivalent to the maximum grain size [35].

The integration of the Eq. (4) was carried out for variable values of a_i , a_f and constant material parameters (m = 3.37, C = $2.12 \cdot 10^{-12}$ m/cycle/(MPa$\sqrt{\text{m}}$)^m [36]). The data were used from crack growth curves for SLM 316L consistent with the specimen orientation. The model output value is significantly affected by the decrease in a_i resulting in a longer number of cycles. The process of nucleation and crack growth to the initial crack length a_i is slow. The propagation of short cracks is irregular. The cracks may be stopped at grain boundaries and other structural barriers of the material at relatively low stress levels. Most of the fatigue life is consumed in the initiation

phase [14]. The initial crack size for stable crack growth is calculated from the threshold stress intensity factor ΔK_{th}:

$$a_i = \frac{1}{\pi}\left(\frac{\Delta K_{th}}{F_p \Delta S}\right)^2 \quad (5)$$

For a material with defects, the crack depth parameter a_i represents to the area of the critical feature detected on the crack surface defined by the Murakami parameter. The equation for a semicircular crack takes the form [37]:

$$a_i = \sqrt{2/\pi}\sqrt{area} \quad (6)$$

The calculated value (a_i = 315.7 μm) is consistent with the defect size for the upper confidence interval of the log-normal distribution, as detailed in Section 3.2. From the observation of the specimen fracture, the final fracture length a_f increases with specimen size. The upward trend of the variable does not significantly affect the output value of the model. The crack propagation at the end of fatigue life is fast enough not noticeably increased the number of cycles. Table 4 shows the results of the analysis for a knee point of the *P-S-N* curve and the variable failure probability. The predicted fatigue strength for the crack initiation phase is slightly lower than the experimental total fatigue life N_f. The initiation phase occupies more than 90% of the fatigue life. The approximate values of the n_s coefficient suggest a minor effect on the stable crack growth phase. The failure mechanism of the crack initiation phase significantly determines the fatigue strength of different sized specimens. The explanation of the phenomenon points to the implementation of a statistical model for material defects.

Table 4. Predicted fatigue strength and n_s coefficient for the crack initiation phase.

Specimen number	Failure probability, P_f [%]	Fatigue strength for $5 \cdot 10^5$ cycles, S_f [MPa]		Size effect coefficient, n_s	
		Total life, N_f	Initiation life, N_i	Total life, N_f	Initiation life, N_i
A02	10	220.6	218.8	1.014	1.016
	50	235.9	234.5	1.009	1.011
	90	249.8	248.6	1.008	1.009
A08	10	217.5	215.2	1	1
	50	233.6	231.8		
	90	247.7	246.2		
A32	10	203.3	200.5	0.934	0.931
	50	220.5	218.3	0.943	0.941
	90	233.5	231.6	0.942	0.940

2.5. Estimation of highly stressed volume

The fatigue failure is dependent on the highly stressed volume (*HSV*) [18]. The fatigue strength is determined by the local volume of material subjected to at least *n*% of the maximum stress. The parameter is commonly estimated empirically for 95% [38, 39], 90% [40, 41, 42], 80% [19, 43, 44]. The approach is implemented for geometrically similar objects in which the local stress state is identical. The model in combination with the weakest

link theory proved the possible good prediction of *P-S-N* curves for variable stress gradient (axial, bending loading) [45]. The approach was implemented to transfer laboratory data to real-world objects under exploitation [46].

A numerical calculation procedure based on FEA is used to determine the *HSV*. The CAD model is consistent with the experimentally tested specimens (Fig. 4). The calculations were carried out in ANSYS using the structural analysis module with constant boundary conditions in the linear-elastic analysis range. 20-node solid elements with three degrees of freedom per node with a square displacement character (SOLID186) were used. The selection of the finite element mesh was dictated by the discretisation error analysis carried out. The upper limit of the *P-S-N* curve stress range was well below the yield strength so an isotropic elastic model of the material was used. The model parameters adopted were consistent with experimental data for SLM 316L steel (Table 1). An axial load was applied along the length of the specimen. Fig. 6 shows example boundary surfaces for four cases of maximum stress percentage. Each surface was determined from the normal stress distribution map along the z-axis. The variable *n*% was determined empirically by measuring the location of the macro-crack. Fig. 7 shows the location of the final crack against the symmetry plane (x-y) of the specimen. The ordinate axis is the normalized normal stress, which correlates to the limit of the highly stressed volume calculated according to FEA. The points represent the measured crack location as a function of specimen size, located on the numerically estimated normal stress curve. Most fatigue cracks do not occur in the centre of the specimen with the smallest cross-sectional area and highest stress. The random crack locations are determined by the local stress gradient and the nominal stress in the specimen section. All observed cracks are localised for *HSV* above 90% of maximum stress. The value was estimated based on the number of specimens according to Table 2.

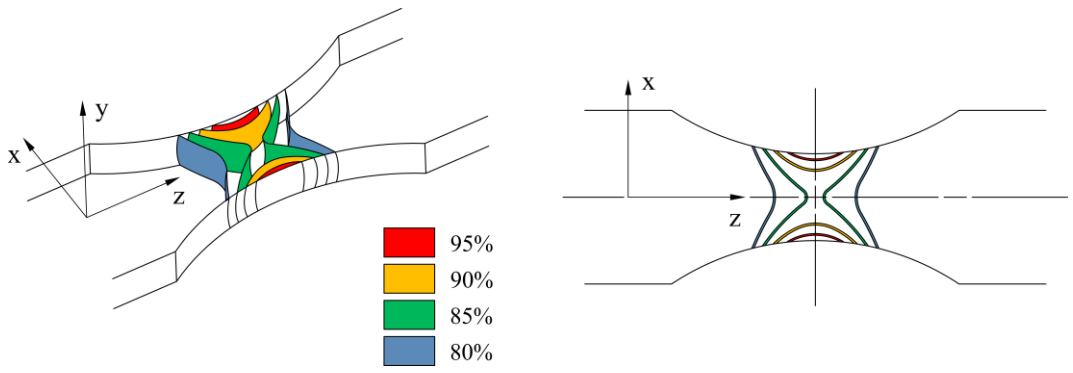

Fig. 6. Surfaces of highly stressed volume depend on the percentage of maximum stress (A08).

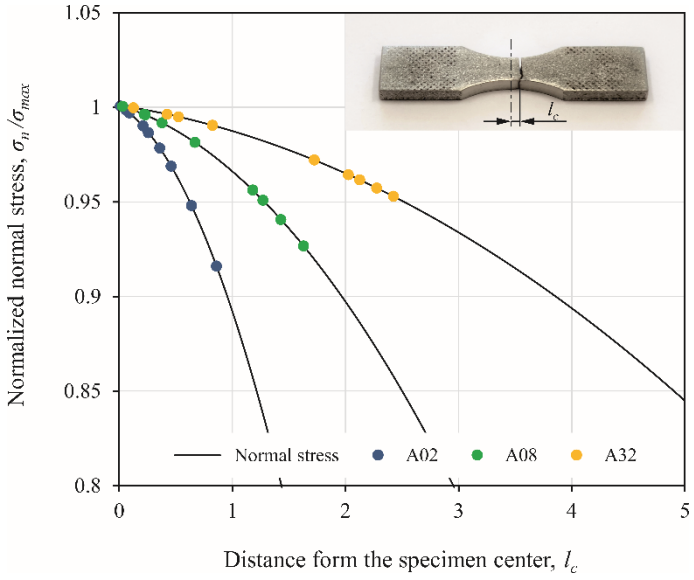

Fig. 7. Location of the final fracture on the numerical curve of normalized normal stress.

3. Proposed size effect model

3.1. General assumptions

The failure mechanism analysis of AM materials suggests the important role of material defects as a factor in premature failure. The noted differences in the locations of experimental *P-S-N* curves for variable sized geometrically similar specimens might be simulated by statistical defect distributions. A larger volume of material determines a higher probability of a critical defect significantly decreasing the fatigue strength. The verification of the assumption was realized by implementing the proposed algorithm according to the identified steps:

- the variability of defect size $\sqrt{area}$ is described by a probabilistic measure represented by a log-normal distribution,
- the randomness of defect location t_b limits *HSV* for experimentally $n\%\sigma_{max}$ and thickness t_d for subsurface volume,
- the stress state in the vicinity of detected surface and subsurface defects is described by a non-local multiaxial criterion,
- the criticality of the defect is calculated for the fatigue criterion threshold and numerical modelling results,
- the random distributions of defects in a range of parameters (*HSV*, $\sqrt{area}$, t_b, ρ_d, defect type) are simulated for a population of numerical specimens,
- the probabilistic scatter bands are predicted for the size effect coefficient calculated from the extreme value statistics of the equivalent normalized stress.

The results are described in detail and discussed in the following sections.

3.2. Defect size

The effect of defect size on fatigue strength is quantified using Murakami empirical fatigue criterion. The model provides an estimate of the experimental fatigue strength for materials containing defects. The approach assumes the use of $\sqrt{area}$ as a geometric parameter for defects and Vickers hardness as a material parameter. The fatigue strength of the knee point percentage curve and mean stress is calculated from the equation [3]:

$$S_f(R) = \frac{d_l\,(HV+120)}{\sqrt{area}^{1/6}}\left(\frac{1-R}{2}\right)^{\alpha_M} \tag{7}$$

$$\alpha_M = 0.226 + HV \cdot 10^{-4} \tag{8}$$

where $\sqrt{area}$ is the defect size parameter, d_l is the location of the defect (surface defect – 1,43; subsurface defect – 1.41; internal defect – 1.56), *HV* is the Vickers hardness and *R* is the stress ratio. The fatigue strength S_f is the threshold stress for the non-propagation of cracks, irrespective of the presence of a defect. Below this value, the crack initiated by the defect stops propagating without causing decohesion of the object. For defects smaller than a certain critical size or their absence, the fatigue strength depends on the failure behaviour of the microstructure in proportion to the hardness.

The defect size controlling fatigue strength is defined as the critical defect initiating failure in a homogenous cyclic stress field. The correlation between fatigue strength and critical defect size is estimated from the Kitagawa Takahashi diagram as a function of power law [47]. The variables ($\sqrt{area}$, S_f) plotted on bi-logarithmic scales can be approximated to linear regression. The defects above the straight line cause failure. The critical defect size for the experimentally tested specimen sizes and fatigue strength for 50% failure probability was calculated using Eq. (7). Table 5 shows the results for each specimen and the parameters of the linear regression equation. The material hardness (*HV* = 235) and the fatigue cycle asymmetry factor *R* = -1 were assumed.

Table 5. Estimated critical defect size from the Murakami model for experimental fatigue strength and variable specimen size.

Parameter	Specimen number			Average value	Linear regression, $logS = k\,log\sqrt{area} + b$	
	A02	A08	A32		*k*	*b*
S_f [MPa]	235.9	233.6	220.5	230.0	-0.167	2.704
$\sqrt{area}$ [µm]	97.6	103.5	146.4	115.8		

The implementation of the Murakami model is aimed to simulate the effect of defect size on the fatigue strength. The number of cracks initiated in defects varies non-deterministically, so the use of a probabilistic model is the basis for further analysis. The variation in defect size is well represented by a log-normal distribution. The probability density function takes the form:

$$f\left(\sqrt{area}\right) = \frac{1}{\sqrt{area}\,\sigma\sqrt{2\pi}} \cdot e^{\left(-\frac{(\ln(\sqrt{area})-\mu)}{2\sigma^2}\right)^2} \quad (9)$$

where μ, σ are the logarithmic normal distribution parameters (size, shape).

Fig. 8 shows the measured defect sizes for each specimen size. Most of the crack origin were located in surface defects (solid points). The prevalence of failure from the surface is a common observation in the presence of defects, especially AM materials. The subsurface defects (empty points) represented a smaller percentage of all cases. The parameter $\sqrt{area}$ is related to the size effect coefficient for a 50% failure probability. A decrease in the coefficient n_s correlates with an increase in defect size. All measured data were estimated with a log-normal distribution (grey solid lines, μ = 4.8, σ = 0.5) independent of specimen size (number of specimen n = 28), assumed as a probabilistic material constant. The mean of the distribution (dashed line, $\sqrt{area}$ = 107.2 µm) is close to the estimated average defect size from Eq. (7) ($\sqrt{area}$ = 115.8 µm). The lower and upper limits of the confidence interval (α_0 = 0.05) are marked with dotted lines. Under the mean of the distribution, the decrease in defect size does not significantly affect the decrease in fatigue strength.

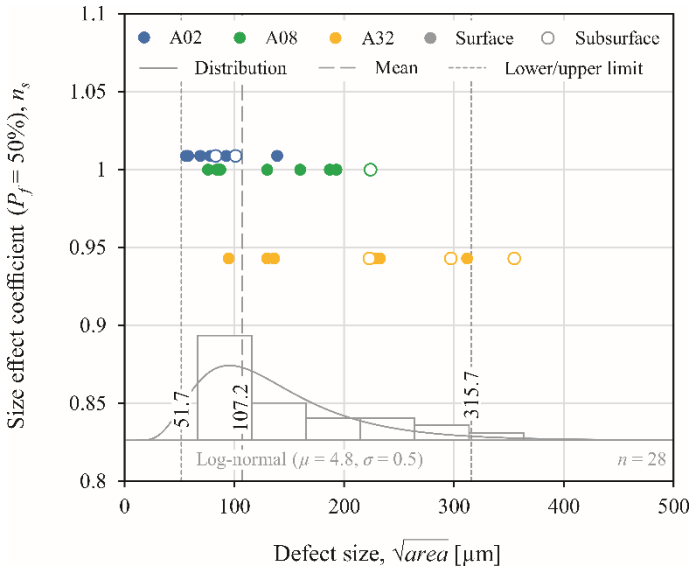

Fig. 8. Size effect coefficient for defect size estimated by log-normal distribution.

3.3. Defects location

The analysis of the failure mechanism indicates the location of the critical defect in the subsurface volume. The thickness of this volume determines the dimension t_d. The parameter is a material property as a function of the localization and size of the critical defect. The dimension t_d shall not be less than the greatest distance of the outermost point of the critical defect from the outer surface. The exact dimension does not significantly affect the outcome in terms of the proposed model. From the point of view of fatigue strength estimation, the distance of the defect (t_b) from the outer specimen surface is more important than the dimension t_d.

Fig. 9 shows an example visualisation of *HSV* estimated numerically for 90%σ_{max} (A08). The enlarged one-quarter geometry (right side of the figure) defines a constant dimension t_d. The volume limit is determined by the specimen geometry along the y-axis and the outer surface of the *HSV* is approximated to a polynomial with y, z elements in the form x = *f*(y,z). The power of the *nth* degree polynomial equation is:

$$f(y,z) = \sum_{i=0}^{n} \sum_{j=0}^{n} a_{ij} y^i z^j \tag{10}$$

where y, z are known points, a_{ij} are coefficients of the polynomial calculated by the method of least squares. A second-order polynomial surface equation was obtained with a matching accuracy of R^2 above 0.95. Table 6 summarizes the numerically calculated *HSV* for t_d independent of specimen size.

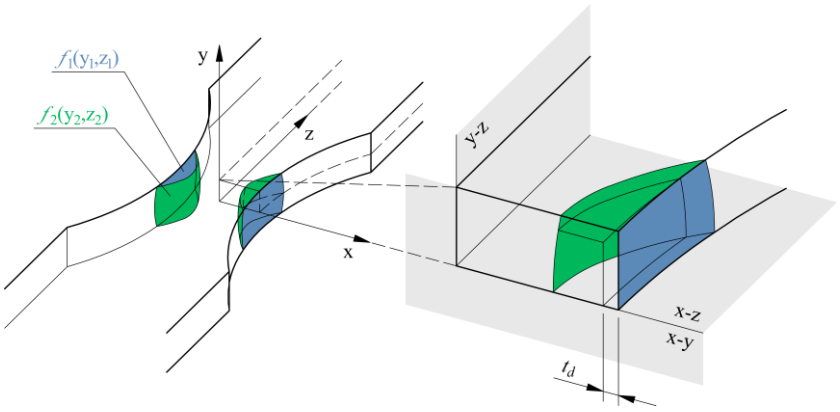

Fig. 9. Highly stressed volume limit for 90%σ_{max} (A08).

Table 6. Numerical value of highly stressed volume 90%σ_{max} for variable specimen size (t_d = const.).

Specimen number	Highly stressed volume, *HSV* [mm^3]
A02	1.12
A08	7.92
A32	40.48

The location of critical defects is determined by random values constrained by the model boundary conditions (equations describing *HSV*). A defect size according to a log-normal distribution (Fig. 8) is assigned to the generated 3D defect location. The idealised geometry of a simplified spherical defect is considered. The method has become widely used for defect modelling for specimens fabricated from aluminium alloys [48, 49], nickel alloys [50], steel [51, 52]. Few examples can be found of structure analysis considering complex microstructure [49, 53] applied to single defect geometry cases. The cross-sectional area of the 3D defect model corresponds to the geometrical parameter $\sqrt{area}$.

To generate a numerical model of the specimen requires determining the average number of defects per volume unit. The spatial density of defect distribution is described by the equation:

$$\rho_d = \frac{V_d\, n_d}{HSV} 100\% \tag{11}$$

where V_d is the average defect volume, n_d is the number of defects, *HSV* is the highly stressed volume. Considering the summarized information from the literature [11] and the energy density for the applied additive manufacturing parameters of 69.4 J/mm^3 (Section 2.1), most of the data is below 2% defect density. The value under 0.5% is qualified as "highly dense" material [54]. The selection of process parameters provides a lower defect density [4]. The values of 0.1%, 0.5% and 2% were selected for further analysis.

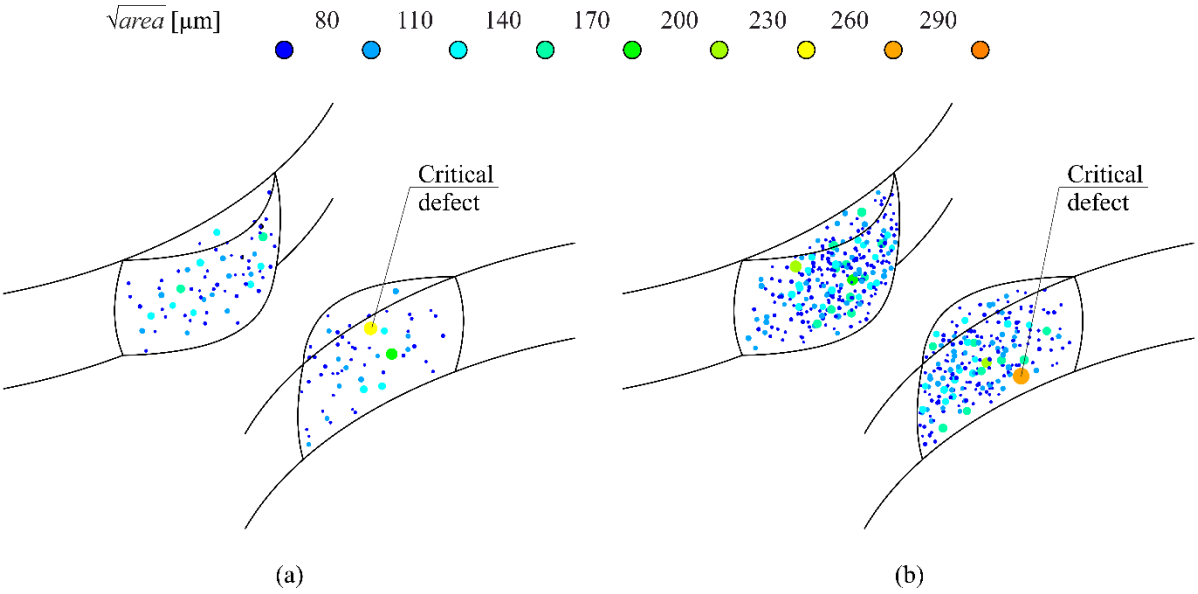

Fig. 10. Visualization of defect distribution in a highly stressed volume 90%σ_{max} as a function of defect density ρ_d (A08): a) 0.5%, b) 2%.

The specified input data was applied to a parametric CAD solid model using a specially provided macro. No data optimisation procedures were used to generate the model. The numerical model is magnified 1000 times to avoid the problems of modelling a micro-scale object. Fig. 10 shows an example visualisation of a CAD model containing randomly distributed defects in the *HSV*. The macro determines the colour of the model depending on the defect size. The scale is divided into intervals corresponding to the estimated log-normal distribution of the $\sqrt{area}$. The visualization shows critical defects for the correlation of the maximum defect size and the shortest distance from the outer surface of the specimen. The definition is general, described in detail in the following sections. The designed procedure allows generating a numerical model for any defect size distribution and specimen size.

3.4. Multiaxial fatigue criterion

The implementation of commonly used approaches comes down to treating the defect as a notch. The fatigue crack initiation is determined by the stress level at the hot spot of the notch and at a certain distance from that

location. In view of the high stress gradient, using a local approach can result in a large scatter of results and lead to predictive data with significant error. The dedicated models use non-local criteria averaging stresses over a point, line, volume [55, 56] or stress area gradient [57]. The local stress averaging procedures shift the distribution towards lower values. An increase in the stress gradient increases the impact of data averaging.

The stress distribution in the vicinity of the defect is defined by the Crossland multiaxial fatigue criterion [23] used in other studies [58, 59, 60]. The calculated equivalent stress is a quantitative measure of defect criticality. The criterion considers the linear combination of the amplitudes of the second invariant of a deviatoric stress tensor $J_{2,a}$ and the maximum hydrostatic stress $J_{1,max}$ over a load cycle, according to the equation:

$$\sigma_{CR} = \sqrt{J_{2,a}} + \alpha_{CR} J_{1,max} \leq \beta_{CR} \tag{12}$$

The stress value $J_{2,a}$ is obtained by double maximisation during the loading period:

$$J_{2,a} = \frac{1}{2\sqrt{2}} \max_{t_I \in T} \left\{ \max_{t_J \in T} \sqrt{\left(\bar{\bar{S}}(t_I) - \bar{\bar{S}}(t_J)\right) : \left(\bar{\bar{S}}(t_I) - \bar{\bar{S}}(t_J)\right)} \right\} \tag{13}$$

where $\bar{\bar{S}}$ is the cyclic stress deviator tensor at two instantaneous times (t_I, t_J) calculated for the maximum and minimum value reached in a sinusoidal cycle. The stress value $J_{1,max}$ is by the equation:

$$J_{1,max} = \frac{1}{3} \max_{t \epsilon T} \{tr(\bar{\bar{\sigma}}(t))\} \tag{14}$$

The material constants α_{CR} and β_{CR} are determined from fatigue tests under two load conditions for unnotched specimens made of reference material. The parameters were calculated for knee point fatigue strength in the fully reversed torsion (τ_w) and fully reversed tension/compression (σ_w), using the following equations:

$$\alpha_{CR} = \frac{3\tau_w}{\sigma_w} - \sqrt{3} \tag{15}$$

$$\beta_{CR} = \tau_w \tag{16}$$

The defect criticality is achieved for a Crossland stress σ_{CR} equal to the threshold parameter β_{CR}. The comparison of results regardless of the level of stress amplitude requires the implementation of normalised equivalent stress calculated according to the equation:

$$\sigma_{CR,n} = \frac{\sigma_{CR}}{\beta_{CR}} \tag{17}$$

The sensitivity of the material to the statistical size effect was described by the n_{sCR} coefficient for the normalized Crossland stress ratio. The same definition of stress is required to correctly determine the coefficient, as follows:

$$n_{sCR} = \frac{\sigma_{CR,n\ max50\%\ A}}{\sigma_{CR,n\ max50\%\ A_0}} \tag{18}$$

where $\sigma_{CR,n\ max50\%}$ is the estimated mean normalised equivalent stress for the reference specimen A_0 and the predicted specimen size A. The probabilistic approach of the proposed model assumes the use of Weibull

distribution for the fatigue strength corresponding to a fixed number of cycles of the *P-S-N* curve. The cumulative distribution function of the fatigue strength is estimated for any specimen size.

3.5. Numerical simulations

To analyse the local stress distribution around the defect depending on the size and location, numerical simulations were carried out using an idealised structure. The computational procedure involves modelling a representative volume element (RVE) [61] consisting of a steel matrix and a spherical defect (void). The object provides information on the local features of the stress distribution in the vicinity of the defect. Fig. 11 shows a model of the RVE geometry in the x-z section plane. The model defines the symmetry of the geometry and boundary conditions in the x-y and x-z planes. The object is a cube with a side of 1500 μm, 5 times the largest defect. The size of the RVE is considered to be the smallest volume represented for the total. In the z-axis direction, a tensile load F equivalent to normal stress was applied to the upper surface of the steel matrix. The variable void parameters adopted are defect size ($\sqrt{area}$) and location along the x-axis (t_b).

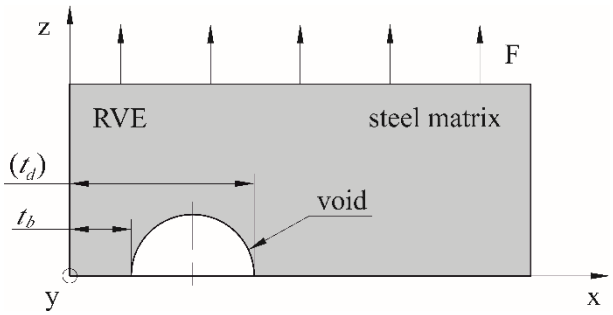

Fig. 11. Boundary conditions for the RVE method of the spherical defect model.

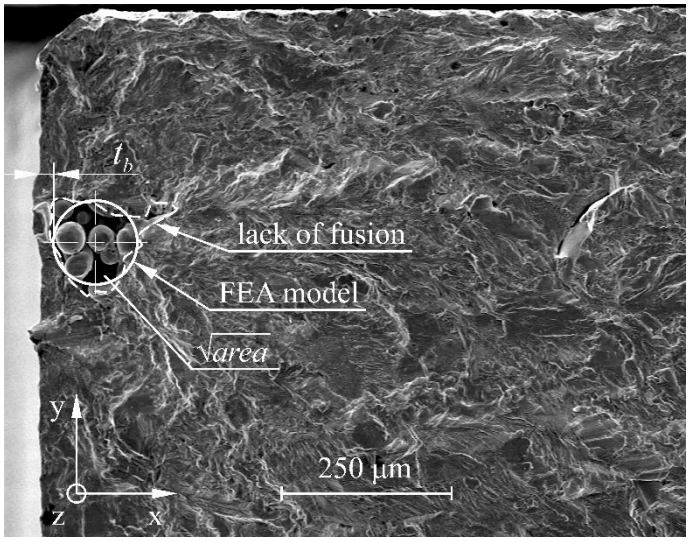

Fig. 12. Example of a subsurface defect on the failure surface of SLM 316L steel.

Fig. 12 shows the defect geometry of the numerical model (solid line) and the actual void (dashed line) observed in SLM 316L steel. The fracture surface follows the normal plane in the direction of the loading. The crack origin occurs in the lack of fusion defect. The parameter $\sqrt{area}$ is measured in the x-y plane. The dimension t_b is a modelled value assumed for the simulation of the numerical defect location. The measurement is defined relative to a simplified void geometry.

The RVE is modelled using the finite element method (FEM) in the ANSYS software environment. The steel matrix is homogeneous materials. 3-D 10-node tetrahedral structural solid elements (SOLID187) with three degrees of freedom in each node (translations in the nodal x, y, and z directions) were applied. The elements have a square displacement characteristics and are suitable for modelling irregular meshes. The CAD model environment was enlarged 100 times to avoid problems caused by the small scale. The verification of the mesh discretization showed no significant effect of further refinement on the result. The acceptable accuracy was obtained for a maximum element size of 5 mm. In the vicinity of the defect refinement mesh. The average value of the element quality factor, i.e. the ratio of volume to edge length for a given element, is equal to 0.82 (a value of 1 indicates a perfect cube). The lower confidence interval for the ratio distribution is above 0.3. The model was generated as a continuum in terms of mesh and deformation. The approach allows the compilation and extension of the model to an infinite area guaranteeing the representativeness of the material. The steel matrix behaves as an elastic-plastic medium with non-linear isotropic hardening (Young's modulus: 170 GPa, Poisson's ratio: 0.3) fitted to the experimental stress-strain curve for stainless steel. The calculations were carried out in the structural analysis module under constant load and reaction conditions. The Crossland equivalent stress components (Eq. (13), (14)) are determined by the non-local method for each integration point of the finite element model.

4. Results and discussion

4.1. Defect criticality

A procedure to estimate the local stress distribution was carried out using the finite element method to determine the influence of selected variables on the defect criticality. The macroscopic stress gradient around the defect depends on the load and the type of defect. The applied local approaches considering hot spot stresses do not result in a safe fatigue strength estimation [57, 62]. Many points are in the criterion failure zone. The non-local method was implemented to average the results for a defined sphere of radius *r* for each numerical data. A similar approach was verified for stainless steel [60] and aluminium alloy [59].

Fig. 13 shows the distribution maps of the normalized maximum principal stress. The views were generated for the same defect size ($\sqrt{area}$ = 200 μm) at two locations (surface defect – Fig. 13a, subsurface defect – Fig.

13b). The critical stress state occurs in the volume region at the largest void diameter measured in the plane normal to the load. The maximum value is determined by the defect location, 2.11, 2.46 for surface and subsurface defect, respectively. In each condition, the extremum occurs in the plane of the smallest section of the steel matrix. The bridge between the subsurface defect and the outer surface determines the increase in local shear stress.

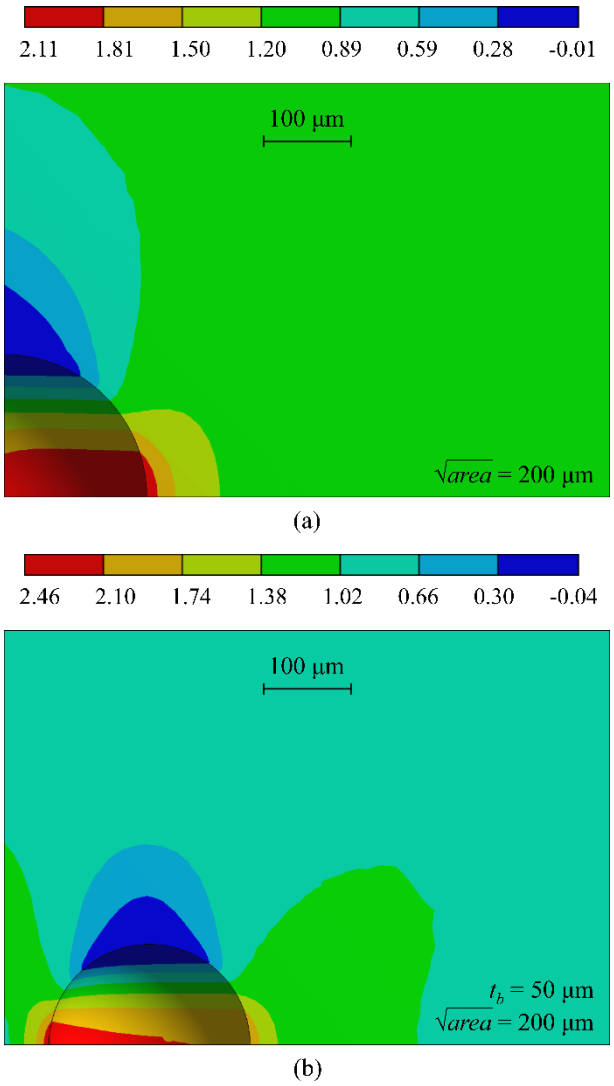

Fig. 13. Normalized maximum principal stress distribution around the void (x-z plane): a) surface defect, b) subsurface defect.

Fig. 14 shows the numerical simulation results for the averaged normalised stresses $J_{2,a}$ and $J_{1,max}$ of the Crossland criterion. The graphical visualization of the criterion is intended to simplify the comparison of results. The sloped continuous line is a criterion threshold. The data above the criterion points to the criticality of the defect. The location of the threshold is determined by the material constants α_{CR} and β_{CR}. The threshold is constant for all test configurations. A single analysis is computed for each variable marked on the graph. The load values and FEA parameters for all simulations are constant. The results in the graphs are shown for data above the nominal

stress. The results were averaged using a volumetric approach with a critical distance for a radius r of 60 μm. The value was estimated for a surface defect of $\sqrt{area}$ = 100 μm. The output result was calculated using an iterative method, followed by data approximation. The threshold line is tangent to this base defect. Fig. 14a shows selected numerical data for variable r in relation to the local method. The assumed radius significantly affects the data averaging due to the significant gradient around the defect.

The Murakami model, Eq. (7) determines the fatigue strength depending on the defect location d_l (surface – 1.43; subsurface – 1.41). The analyses were conducted for similar conditions to evaluate the correctness of the numerical model prediction. Fig. 14b shows data for a surface defect of variable $\sqrt{area}$. The criticality of the defect increases with void size. The data follow the same trend in the direction of normal stress. A significant increase in the shear stress amplitude $J_{2,a}$ was not noted. The distribution is consistent with the basic theory of normal stress state in a notch. The following set of calculations compares results for subsurface defects of the variable $\sqrt{area}$ (Fig. 14c) and the dimension t_b (Fig. 14d). The range of defect sizes corresponds to the estimated log-normal distribution (Fig. 8). The increase in the defect criticality is proportional to the defect size. The behaviour of the numerical model is in line with the Murakami model. The correlation is particularly noticeable in the shear stress amplitude range. A decrease in the value $J_{2,a}$ indicates a decrease in the criticality for subsurface defects translating into an increase in fatigue strength. The high sensitivity of fatigue endurance was also obtained for variable thickness t_b. The crack initiation is significantly affected by the location of the subsurface defect. A reduction in the depth of defect location causes a decrease in fatigue strength.

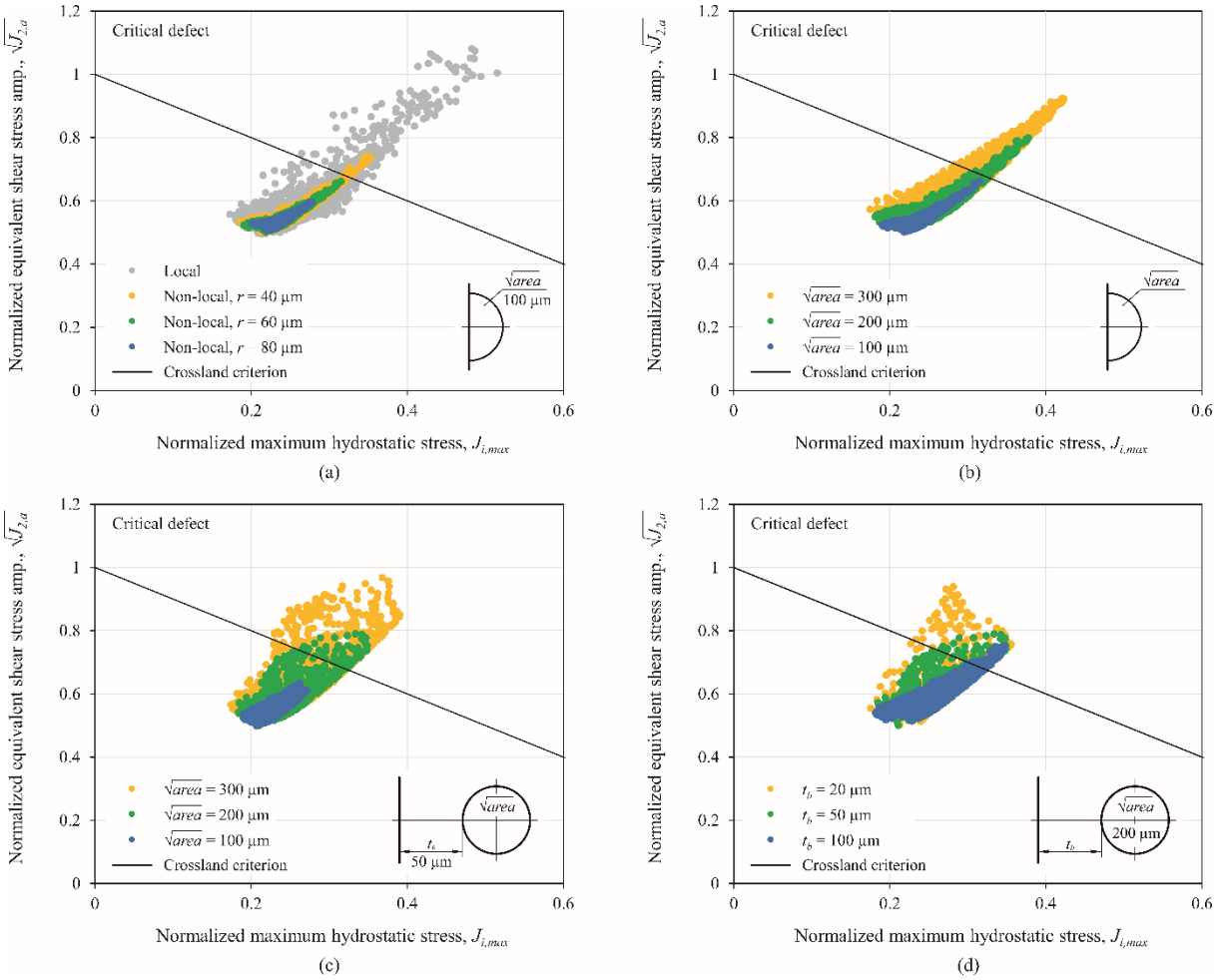

Fig. 14. Comparison of the normalized stress distribution with the Crossland criterion, variable: a) surface defect – data averaging radius r, b) surface defect – $\sqrt{area}$, c) subsurface defect – $\sqrt{area}$, d) subsurface defect – t_b.

The FEA results show a significant increase in the non-local stress distribution components of the Crossland criterion for the variable of defect location and size. The Murakami model does not take into account the defect location relative to the specimen surface. The largest defect is not necessarily critical. The model for estimating the size effect should take into account the sensitivity of fatigue strength to the thickness between the specimen surface and the subsurface defect. The defect criticality was defined using the normalised Crossland equivalent stress $\sigma_{CR,n}$ according to Eq. (17). The maximum stress values were taken on the defect surface for selected configurations of the statistical model predictors ($\sqrt{area}$, t_b). The effect of variables was described by approximating the data using multivariate non-linear regression analysis. The equation for the quadratic area regression model for two variables takes the form:

$$\sigma_{CR,n} = \beta_0 + \beta_1\sqrt{area} + \beta_2 t_b + \beta_3\sqrt{area}t_b + \beta_4\sqrt{area}^2 + \beta_5 {t_b}^2 \quad (19)$$

where β_0 is the intercept, $\beta_1 - \beta_5$ are the regression coefficients (1-α_0 = 0.95). Table 7 contains the results for the second-order matching model. The high value of the coefficient of determination (surface – R^2 = 0.99, subsurface

– R^2 = 0.93) indicates a good fit for the numerical data. The regression coefficients are statistically significant (*p*-value is less than 0.05).

Table 7. Coefficients of the analytical model for the output variable $\sigma_{CR,n}$.

Defect	β_0	β_1	β_2	β_3	β_4	β_5
Surface	0.7962	0.0018	-	-	-	-
Subsurface	0.8314	0.0026	-0.0054	$-4.6664 \cdot 10^{-6}$	$5.57 \cdot 10^{-8}$	$3.4855 \cdot 10^{-5}$

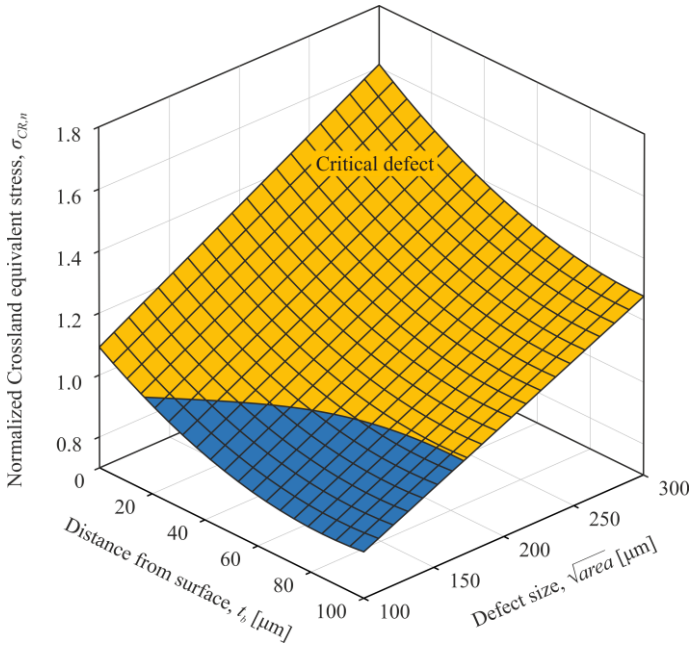

Fig. 15. Approximated equivalent stress for subsurface defect numerical results of defect size and distance from the specimen surface.

Fig. 15 shows a graphical visualisation of the surface for a subsurface defect. The approximation range of the model corresponds to the limits of the system axes. The yellow area shows the Crossland criterion threshold exceeded (above 1). The proposed analytical model implements the maximum criticality of the defect occurring in the calculated *HSV* of the specimen depending on the size. The procedure of applying the approximation function to determine the stress $\sigma_{CR,n}$ significantly reduces the computation time than the CAD model generation and FEM calculation. The model input data are the same as shown in Fig. 10. The defect criticality is calculated analytically by repeating the procedure *n* times for any number and size of *HSV*. The proposed definition of the tested material provides a statistical characterization of the size effect.

4.2. Prediction of fatigue strength

The proposed approach aims to simulate a critical defect in specimens of three different sizes, consistent with Table 2. Fig. 16 shows examples of defect locations in numerical specimens for variable defects density (ρ_d = 0.5%; 2%). The abscissa axis determines the defect location as a function of specimen size for 90%σ_{max}. The value

is measured along the z-axis of the specimen (Fig. 9). Each point is a defect found in *HSV* in the subsurface layer. The result is generated for the defect size distribution (Fig. 8) and the range of defect location consistent with the numerical analysis for $t_{b,max}$ = 100 µm (value independent of specimen size). According to the FEA, the critical defects above this value were not observed for the assumed defect size range. The stress $\sigma_{CR,n}$ was calculated analytically according to Eq. (19) for a randomly generated (Mersenne Twister algorithm) defect location and size. The form of the model (surface defect, subsurface defect) was determined depending on the randomly generated defect location. The mean value of the stress $\sigma_{CR,n}$ calculated for all points correlates with the median of the distribution. The stress $\sigma_{CR,n\,max}$ (dashed line) for a critical defect depends on the specimen size and defects density.

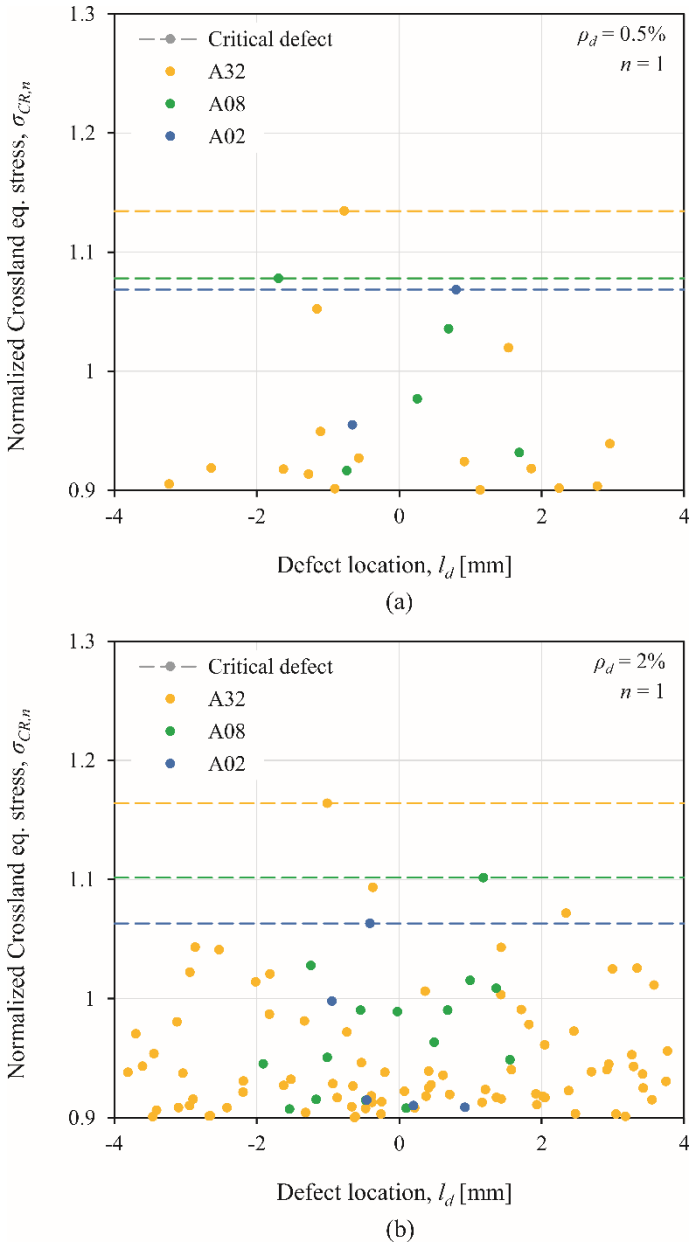

Fig. 16. Critical defects in *HSV* as a function of specimen size, defect density ρ_d: a) 0.5%, b) 2%.

The model validation was carried out for the experimental log-normal distribution of defect sizes (Fig. 8) and the estimated data based on the proposed approach. Fig. 17 shows the data set determined as a cumulative distribution function P and the reduced variance -ln(-ln(P)). The $\sqrt{area}$ describes the extreme value statistic. A good fit of the data was obtained for linear regression. The agreement between the experimental and estimated values is the result of fitting the input log-normal distribution (μ = 2.2, σ = 0.9) to the output. The model input quantities result in correct estimation of the ratio of the number of surface (solid points) and subsurface (empty points) defects. The type of defect is important due to the selection of the analytical model, Eq. (19).

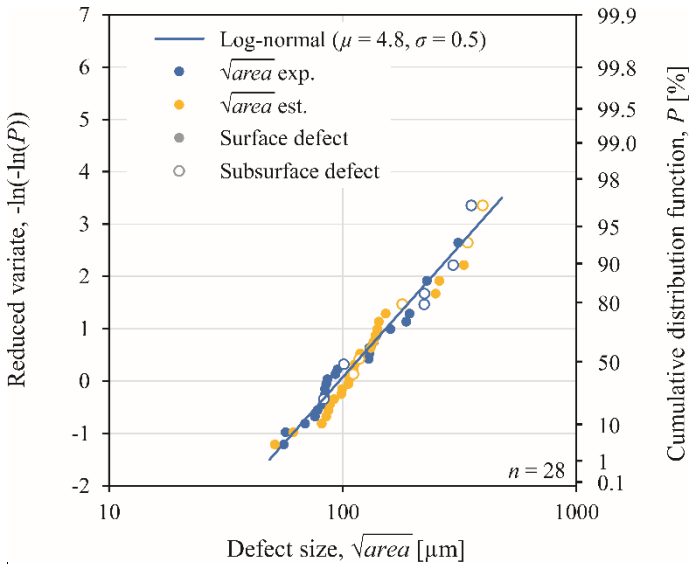

Fig. 17. Comparison of extreme value distributions for experimental and estimated defect size.

The stress $\sigma_{CR,n\ max}$ was calculated for a population of numerical specimens, indexed as j = 1…n, where n = 100. Fig. 18 shows an example of the simulation results for variable defect density. The values for randomly generated data are classified starting from the smallest, according to the relation:

$$\sigma_{CR,n\ max,1} \leq \sigma_{CR,n\ max,2} \leq \cdots \leq \sigma_{CR,n\ max,n} \tag{20}$$

A linear regression (solid line) was approximated only for critical defects. Under the threshold of the Crossland criterion, a defect can cause failure but not increase fatigue strength compared to a defect stress $\sigma_{CR,n\ max}$ of 1. The approach defines non-linearity of the model for small *HSV*. The stress $\sigma_{CR,n\ max50\%}$ (Eq. (18)) for a 50% probability can be predicted from the intersection of the solid distribution lines. The dashed lines show the output data for specimens A02, A08, A32. The expected value increases with specimen size, assuming the same distribution of defects. A smaller scatter of stress $\sigma_{CR,n\ max50\%}$ was observed for a defect density of 0.5%. The stress $\sigma_{CR,n\ max50\%}$ dependent on specimen size and defect density is the result of the sum of defect volumes. The variable is the input quantity for generating the numerical model of the specimen.

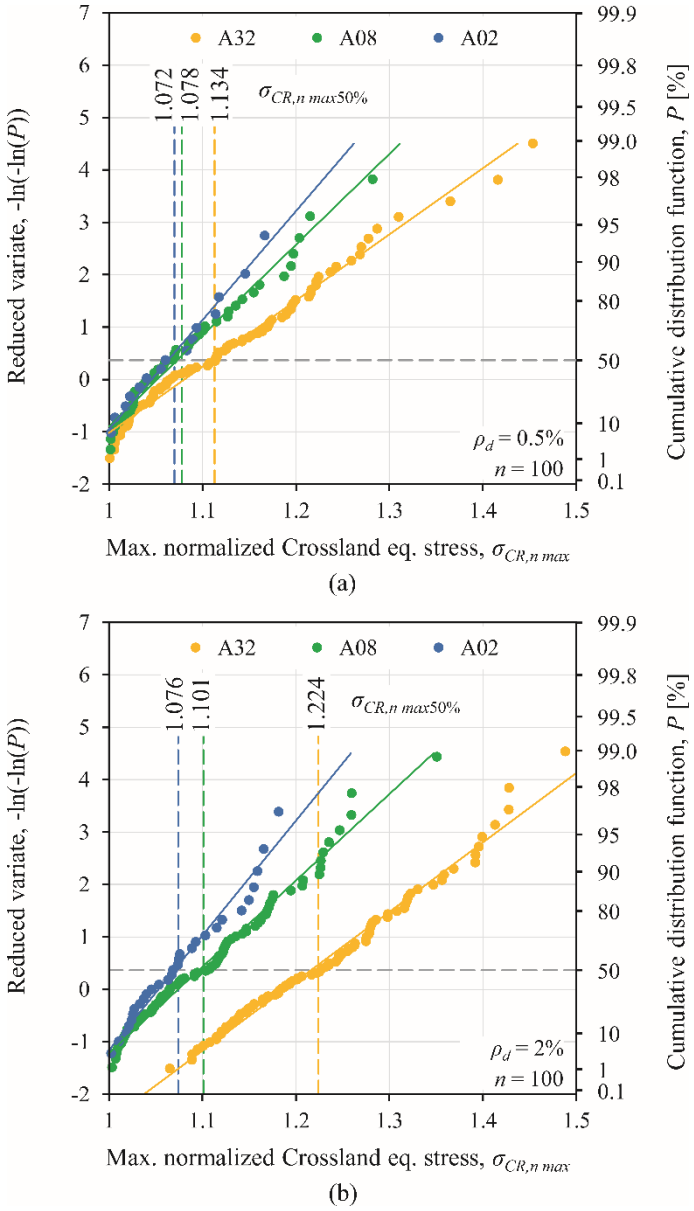

Fig. 18. Comparison of extreme value distributions of equivalent stress for variable specimen size and defect density ρ_d: a) 0.5%, b) 2%.

Fig. 19 shows the correlation of the stress $\sigma_{CR,n\ max50\%}$ and the highly stressed volume. The points were generated for a population of the specimens. The stress was estimated according to the procedure described in the previous paragraph (Fig. 18). The selected range was approximated to a linear form (solid line) in a bi-logarithmic system. The determination coefficient R^2 is above 0.99 for both defect densities. The lower range of the data is characterized by a plateau, peaking at a stress of 1.07. The nonlinearity of the model (dotted line) simulates an unobserved size effect for small *HSV*. The numerically calculated *HSV* (Table 6) is marked with a dashed line. The logarithmic correlation between stress $\sigma_{CR,n\ max50\%}$ and *HSV* determines the significant variation of parameters up to a certain limit. The decrease in fatigue strength for a large object volume is minor. The stress $\sigma_{CR,n\ max50\%}$ were determined for *HSV* of each specimen (A02, A08, A32). The stress ratio for the two specimen sizes is defined

as the size effect coefficient n_{sCR}, according to Eq. (18). The input data for the reference specimen ($\sigma_{CR,n\ max50\%\ A0}$) are the results for A08. The output data is the Weibull distribution of the fatigue strength for specimens A02, A32. The proposed approach is implantable for a non-linear model of the stress $\sigma_{CR,n\ max50\%}$ and *HSV*. Table 8 contains the results of the fatigue strength estimation for selected failure probabilities of 10%, 50%, 90% and relative error. The six prediction combinations were derived from two specimen sizes (A02, A32) and three defect densities of 0.1%, 0.5%, 2%. Visible differences were observed in the analysed data. A better fit of the predicted data was obtained for a defect density of 0.5%. The analytical value $S_{pred.}$ is close to the experimental fatigue strength S_f. The average relative error values are 1.9%, 0.6% and 2.8%, respectively for 0.1%, 0.5% and 2%.

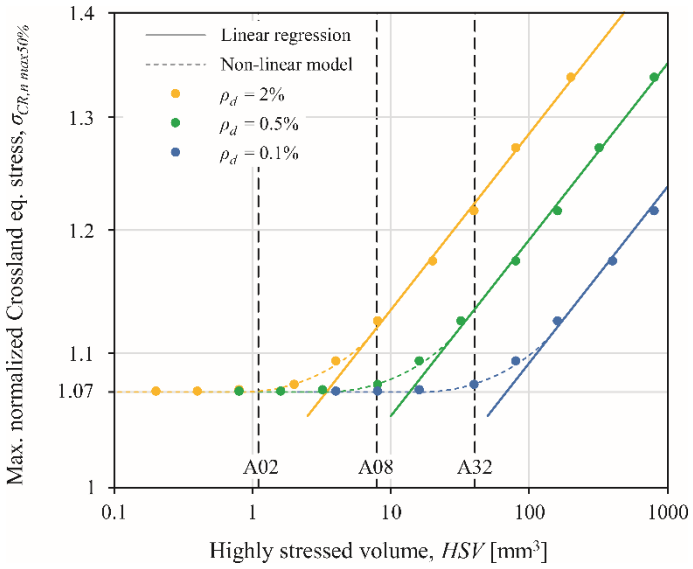

Fig. 19. Approximation of the predicted equivalent stress for a highly stressed volume.

Table 8. Experimental results and predicted values of fatigue strength.

Specimen number	Failure probability, P_f [%]	Experimental fatigue strength, S_f [MPa]	Predicted fatigue strength, $S_{pred.}$ [MPa] (Relative error [%])		
			ρ_d = 0.1%	ρ_d = 0.5%	ρ_d = 2%
A02	10	220.6	219.0 (-0.7)	218.6 (-0.9)	222.6 (0.9)
	50	235.9	235.2 (-0.3)	234.8 (-0.4)	239.1 (1.3)
	90	249.8	249.5 (-0.1)	249.0 (-0.2)	253.6 (1.5)
A32	10	203.3	211.7 (4.1)	205.9 (1.2)	195.7 (-3.7)
	50	220.5	227.5 (3.2)	221.1 (0.3)	210.2 (-4.6)
	90	233.5	241.2 (3.3)	234.5 (0.4)	222.9 (-4.5)

Fig. 20 shows a graphical visualisation of the Weibull cumulative distribution function for fatigue life $5 \cdot 10^5$ cycles. The points are experimental values for the chosen failure probability P_f. The solid line shows the result for the distribution determined from Eq. (1). The data transfer for a specimen of any size is carried out using a cumulative Weibull distribution and a correction coefficient for a variable fatigue strength S_f and a constant value of the aspect ratio α. The dashed lines were estimated based on the proposed probabilistic size effect model for all

analysed defect density. The plot shows that the model prediction for 0.5% agrees well with experimental results for probabilistic scatter bands. A similar fatigue strength estimation errors were obtained for the extreme failure probability. The calculation error usually increases as the *HSV* ratio of the predicted specimen to the reference specimen increases. The correlation is visible for 2%. The errors are significantly larger for A32.

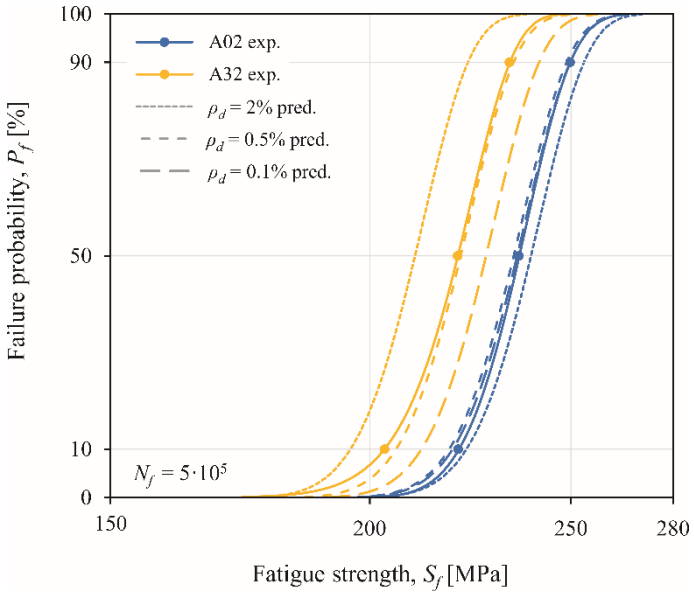

Fig. 20. Weibull cumulative distribution function of experimental and predicted fatigue strength for variable defect density.

5. Conclusion

The paper proposes statistical modelling of size effects for SLM 316L stainless steel. The point of the analyses is the noted correlation of specimen size and the location of the *P-S-N* curves for variable defect size. The simulations of selected factors on the fatigue fracture process, including numerical calculations of model variables, allowed us to propose the following conclusions:

- The evaluation of the individual phases of the failure process did not show the influence of stable crack growth on the size effect. The change in crack end length for specimens varying in size does not significantly affect the estimated number of cycles. The propagation at the final stage for a long crack takes a small percentage of the total fatigue life. The modelling of size effects requires consideration of the failure mechanism during the initiation phase.
- The FEA indicated an increase in the components of the non-local stress distribution of the Crossland criterion around the defect for varying defect location and size. The approximation of the numerical results obtained a good fit to the regression model. The procedure enabled the generation of critical defects in *HSV* depending on the specimen size. The predicted fatigue strength is determined by the n_s coefficient calculated from the simulated extreme value distributions of the equivalent stress.

- The proposed model shows a strong ability to predict the statistical size effect for AM of stainless steel. The defect density determines the size effect behaviour. The defect size gradient depends on the specimen size. For selected distribution parameters, the simulated fatigue strength change correlates well with experimental data (average relative error equal to 0.6%). Increasing the accuracy of the model can be achieved by modelling the natural spread of the experimental data for the shape factor of the Weibull distribution. The approach requires implantation for engineering calculations recommending the use of fatigue characteristics with low failure probability.

Acknowledgments

The studies were financially supported from the project 2021/05/X/ST5/00076 funded by the Polish National Science Centre (NCN).

References

1 Kloos KH, Buch A, Zankov D. Pure geometrical size effect in fatigue tests with constant stress amplitude and in programme tests. Materialwissenschaft und Werkstofftechnik 1981;12:40–50. https://doi.org/10.1002/mawe.19810120205

2 Vollertsen F. Categories of size effects. Production Engineering – Research and Development 2008;2:377–383. https://doi.org/10.1007/s11740-008-0127-z

3 Murakami Y. Metal Fatigue: Effects of small defects and nonmetallic inclusions. Elsevier 2002. https://doi.org/10.1016/C2016-0-05272-5

4 Andreau O, Pessard E, Koutiri I, Penot J-D, Dupuy C, Saintier N, Peyre P. A competition between the contour and hatching zones on the high cycle fatigue behaviour of a 316L stainless steel: Analyzed using X-ray computed tomography. Materials Science and Engineering A 2019;757;146–159. https://doi.org/10.1016/j.msea.2019.04.101

5 Andreau O, Pessard E, Koutiri I, Peyre P, Saintier N. Influence of the position and size of various deterministic defects on the high cycle fatigue resistance of a 316L steel manufactured by laser powder bed fusion. International Journal of Fatigue 2021;143:105930. https://doi.org/10.1016/j.ijfatigue.2020.105930

6 Blinn B, Krebs F, Ley M, Teutsch R, Beck T. Determination of the influence of a stress-relief heat treatment and additively manufactured surface on the fatigue behavior of selectively laser melted AISI 316L by using efficient short-time procedures. International Journal of Fatigue 2020;131:105301. https://doi.org/10.1016/j.ijfatigue.2019.105301

7 Dastgerdi JN, Jaberi O, Remes H. Influence of internal and surface defects on the fatigue performance of additively manufactured stainless steel 316L. International Journal of Fatigue 2022;163:107025. https://doi.org/10.1016/j.ijfatigue.2022.107025

8 Pessard E, Lavialle M, Laheurte P, Didier P, Brochu M. High-cycle fatigue behavior of a laser powder bed fusion additive manufactured Ti-6Al-4V titanium: Effect of pores and tested volume size. International Journal of Fatigue 2021;149;.106206. https://doi.org/10.1016/j.ijfatigue.2021.106206

9 Shrestha R, Simsiriwong J, Shamsaei N. Fatigue behavior of additive manufactured 316L stainless steel parts: Effects of layer orientation and surface roughness. Additive Manufacturing 2019;28:23–38. https://doi.org/10.1016/j.addma.2019.04.011

10 Zeng F, Yang Y, Qian G. Fatigue properties and S-N curve estimating of 316L stainless steel prepared by SLM. International Journal of Fatigue 2022;162:106946. https://doi.org/10.1016/j.ijfatigue.2022.106946

11 Zhang M, Sun C-N, Zhang X, Goh PC, Wei J, Hardacre D, Li H. Fatigue and fracture behaviour of laser powder bed fusion stainless steel 316L: Influence of processing parameters. Materials Science & Engineering A 2017;703:251–261. https://doi.org/10.1016/j.msea.2017.07.071

12 Kocańda S. Fatigue failure of metals. WNT;1978.
13 Tomaszewski T. Statistical size effect in fatigue properties for mini-specimens. Materials 2020;13(10):2384. https://doi.org/10.3390/ma13102384
14 Makkonen M. Predicting the total fatigue life in metals. International Journal of Fatigue 2009;31:1163–1175. https://doi.org/10.1016/j.ijfatigue.2008.12.008
15 Shao C, Cui H, Lu F, Li Z. Quantitative relationship between weld defect characteristic and fatigue crack initiation life for high-cycle fatigue property. International Journal of Fatigue 2019;123:238–247. https://doi.org/10.1016/j.ijfatigue.2019.02.028
16 Deng GJ, Tu ST, Wang QQ, Zhang XC, Xuan FZ. Small fatigue crack growth mechanisms of 304 stainless steel under different stress levels. International Journal of Fatigue 2014;64:14–21. https://doi.org/10.1016/j.ijfatigue.2014.01.027
17 Weibull W. A statistical theory of the strength of materials. R. Swedish Inst. Eng. Res. 1939;151.
18 Kuguel R. A relation between theoretical stress concentration factor and fatigue notch factor deduced from the concept of highly stressed volume. ASTM 1961;61:732–748.
19 Ai Y, Zhu SP, Liao D, Correia JAFO, De Jesus AMP, Keshtegar B. Probabilistic modelling of notch fatigue and size effect of components using highly stressed volume approach. International Journal of Fatigue 2019;127:110–119. https://doi.org/10.1016/j.ijfatigue.2019.06.002
20 Makkonen M. Statistical size effect in the fatigue limit of steel. International Journal of Fatigue 2001;23:395–402. https://doi.org/10.1016/S0142-1123(01)00003-2
21 Carpinteri A. Scaling laws and renormalization groups for strength and toughness of disordered materials. International Journal of Solids and Structures 1994;31:291–302. https://doi.org/10.1016/0020-7683(94)90107-4
22 Tomaszewski T, Sempruch J. Fatigue life prediction of aluminium profiles for mechanical engineering. Journal of Theoretical and Applied Mechanics 2017;55(2):497–507. https://doi.org/10.15632/jtam-pl.55.2.497
23 Crossland B. Effect of large hydrostatic pressures on the torsional fatigue strength of fan alloy steel. Proceedings Of The International Conference On Fatigue Of Metals 1956;138–149.
24 Gumbel EJ. Statistics of Extremes. Columbia University Press 1958.
25 ISO 6892-1:2016. Metallic Materials-Tensile Testing-Part 1: Method of Test at Room Temperature.
26 ISO-1099. Metallic Materials-Fatigue Testing-Axial Force-Controlled Method.
27 ISO-12107. Metallic Materials-Fatigue Testing-Statistical Planning and Analysis of Data.
28 Sonsino CM. Course of SN-curves especially in the high-cycle fatigue regime with regard to component design and safety. International Journal of Fatigue 2007;29(12):2246–2258. https://doi.org/10.1016/j.ijfatigue.2006.11.015
29 Tomaszewski T, Sempruch J. Determination of the fatigue properties of aluminum alloy using mini specimen. Fatigue Failure and Fracture Mechanics 2012;726:63–68. https://doi.org/10.4028/www.scientific.net/MSF.726.63
30 Dowling NE. Mechanical Behavior of Materials: Engineering Methods for Deformation Fracture and Fatigue. Pearson Education Limited 2013.
31 Santus C, Taylor D. Physically short crack propagation in metals during high cycle fatigue. International Journal of Fatigue 2009;31:1356–1365. https://doi.org/10.1016/j.ijfatigue.2009.03.002
32 Mughrabi H. Microstructural mechanisms of cyclic deformation, fatigue crack initiation and early crack growth. Philosophical Transactions of The Royal Society A Mathematical Physical and Engineering Sciences 2015;373:20140132. https://doi.org/10.1098/rsta.2014.0132
33 McClung RC, Francis WL, Hudak Jr SJ. A new approach to fatigue life prediction based on nucleation and growth. Proceedings of 9th International Fatigue Congress (Fatigue 2006). Elsevier 2006.
34 Murakami Y, Endo M. Effects of Hardness and Crack Geometries of ΔKth of Small Cracks Emanating from Small Defects. Mechanical Engineering Publications 1986;275–293.
35 Xie C, Wu S, Yu Y, Zhang H, Hu Y, Zhang M, Wang G. Defect-correlated fatigue resistance of additively manufactured Al-Mg4.5Mn alloy with in situ micro-rolling. Journal of Materials Processing Technology 2021;291:117039. https://doi.org/10.1016/j.jmatprotec.2020.117039

36 Riemer A, Leuders S, Thöne M, Richard HA, Tröster T, Niendorf T. On the fatigue crack growth behavior in 316L stainless steel manufactured by selective laser melting. Engineering Fracture Mechanics 2014;120:15–25. https://doi.org/10.1016/j.engfracmech.2014.03.008

37 Romano S, Brückner-Foit A, Brandão A, Gumpinger J, Ghidini T, Beretta S. Fatigue properties of AlSi10Mg obtained by additive manufacturing: Defect-based modelling and prediction of fatigue strength. Engineering Fracture Mechanics 2018; 187:165–189. https://doi.org/10.1016/j.engfracmech.2017.11.002

38 Lin CK, Lee WJ. Effects of highly stressed volume on fatigue strength of austempered ductile irons. International Journal of Fatigue 1998;20(4):301–7. https://doi.org/10.1016/S0142-1123(97)00134-5

39 Sonsino CM, Fischer G. Local assessment concepts for the structural durability of complex loaded components. Materialwissenschaft und Werkstofftechnik 2005;36(11):632–641. https://doi.org/10.1002/mawe.200500932

40 Härkegård G, Halleraker G. Assessment of methods for prediction of notch and size effects at the fatigue limit based on test data by Böhm and Magin. International Journal of Fatigue 2010;32:1701–1709. https://doi.org/10.1016/j.ijfatigue.2010.03.011

41 Van Hooreweder B, Moens D, Boonen R, Sas P. Fatigue strength analysis of notched aluminium specimens using the highly stressed volume method. Fatigue and Fracture of Engineering Materials and Structures 2012;35(2):154–159. https://doi.org/10.1111/j.1460-2695.2011.01602.x

42 Wang R, Li D, Hu D, Meng F, Liu H, Ma Q. A combined critical distance and highlystressed volume model to evaluate the statistical size effect of the stress concentrator on low cycle fatigue of TA19 plate. International Journal of Fatigue 2017;95:8–17. https://doi.org/10.1016/j.ijfatigue.2016.10.003

43 Lipp K, Baumgartner J, Beiss P. Fatigue design of sintered steel components: effect of stress concentrations and mean stresses on local strength using highest stressed volume approach. Powder Metall 2014;56(5):337–341. https://doi.org/10.1179/0032589913Z.000000000141

44 El Khoukhi D, Morel F, Saintier N, Bellett D, Osmond P, Le VD, Adrien J. Experimental investigation of the size effect in high cycle fatigue: Role of the defect population in cast aluminium alloys. International Journal of Fatigue 2019;129:105222. https://doi.org/10.1016/j.ijfatigue.2019.105222

45 Tomaszewski T, Strzelecki P, Mazurkiewicz A, Musiał J. Probabilistic estimation of fatigue strength for axial and bending loading in high-cycle fatigue. Materials 2020;13(5):1148. https://doi.org/10.3390/ma13051148

46 Tomaszewski T. Fatigue life analysis of steel bicycle frame according to ISO 4210. Engineering Failure Analysis 2021;122:105195. https://doi.org/10.1016/j.engfailanal.2020.105195

47 Kitagawa H, Takahashi S. Fracture mechanics approach to very small crack growth and to the threshold condition. Trans Jpn Soc Mech Engng A 1979;45(399):1289–1303. https://doi.org/10.1299/kikaia.45.1289

48 Li P, Lee PD, Maijer DM, Lindley TC. Quantification of the interaction within defect populations on fatigue behavior in an aluminum alloy. Acta Materialia 2009;57:3539–3548. https://doi.org/10.1016/j.actamat.2009.04.008

49 Gao YX, Yi JZ, Lee PD, Lindley TC. The effect of porosity on the fatigue life of cast aluminium-silicon alloys. Fatigue and Fracture of Engineering Materials and Structures 2004;27:559–570. https://doi.org/10.1111/j.1460-2695.2004.00780.x

50 Jiang W, Yao W, Li P, Luo P. A fatigue life prediction method distinguishing fracture modes for Ni-based single crystal superalloys considering porosity defect. Theoretical and Applied Fracture Mechanics 2021;112:102883. https://doi.org/10.1016/j.tafmec.2020.102883

51 Melander A, Gustavsson A. An FEM study of driving forces of short cracks at inclusions in hard steels. International Journal of Fatigue 1996;18(6):389–399. https://doi.org/10.1016/0142-1123(96)00069-2

52 Nakasone Y, Nishiyama H, Nojiri T. Numerical equivalent inclusion method: a new computational method for analyzing stress fields in and around inclusions of various shapes. Materials Science and Engineering A 2000; 285(1–2):229–238. https://doi.org/10.1016/S0921-5093(00)00637-7

53 Vignal V, Oltra R, Josse C. Local analysis of the mechanical behaviour of inclusions-containing stainless steels under straining conditions. Scripta Materialia 2003;49:779–784. https://doi.org/10.1016/S1359-6462(03)00411-1

54 Ronneberg T, Davies CM, Hooper PA. Revealing relationships between porosity, microstructure and mechanical properties of laser powder bed fusion 316L stainless steel through heat treatment. Materials & Design 2020;189;108481. https://doi.org/10.1016/j.matdes.2020.108481

55 Taylor D. Geometrical effects in fatigue: a unifying theoretical model. International Journal of Fatigue 1999;21(5):413–420. https://doi.org/10.1016/S0142-1123(99)00007-9
56 Taylor D. Prediction of fatigue failure location on a component using a critical distance method. International Journal of Fatigue 2000;22(9):735–742. https://doi.org/10.1016/S0142-1123(00)00062-1
57 Nadot Y, Billaudeau T. Multiaxial fatigue limit criterion for defective materials. Engineering Fracture Mechanics 2006;73(1):112–133. https://doi.org/10.1016/j.engfracmech.2005.06.005
58 Mu P, Nadot Y, Nadot-Martin C, Chabod A, Serrano-Munoz I, Verdu C. Influence of casting defects on the fatigue behavior of cast aluminum AS7G06-T6. International Journal of Fatigue 2014;63:97–109. https://doi.org/10.1016/j.ijfatigue.2014.01.011
59 Bonneric M, Brugger C, Saintier N. Investigation of the sensitivity of the fatigue resistance to defect position in aluminium alloys obtained by Selective laser melting using artificial defects. International Journal of Fatigue 2020;134:105505. https://doi.org/10.1016/j.ijfatigue.2020.105505
60 El May M, Saintier N, Palin-Luc T, Devos O. Non-local high cycle fatigue strength criterion for metallic materials with corrosion defects. Fatigue and Fracture of Engineering Materials and Structures 2015;38(9):1017–1025. https://doi.org/10.1111/ffe.12329
61 Hill R. Elastic properties of reinforced solids: Some theoretical principles. Journal of the Mechanics and Physics of Solids 1963;11:357–372. https://doi.org/10.1016/0022-5096(63)90036-X
62 Dehmani H, Brugger C, Palin-Luc T, Mareau C, Koechlin S, Study of the contribution of different effects induced by the punching process on the high cycle fatigue strength of the M330-35A electrical steel. Procedia Structural Integrity 2016;2:3256–3263. https://doi.org/10.1016/j.prostr.2016.06.406